nature physics

LETTERS

PUBLISHED ONLINE: 26 JUNE 2017 | DOI: 10.1038/NPHYS4174

Quantum spin Hall state in monolayer 1T′-WTe_2

Shujie Tang[1,2,3,4,5†], Chaofan Zhang[1,2†], Dillon Wong[6], Zahra Pedramrazi[6], Hsin-Zon Tsai[6], Chunjing Jia[1,2], Brian Moritz[1], Martin Claassen[1], Hyejin Ryu[3,7,8], Salman Kahn[6], Juan Jiang[3,5,9], Hao Yan[1,2], Makoto Hashimoto[10], Donghui Lu[10], Robert G. Moore[1,2], Chan-Cuk Hwang[9], Choongyu Hwang[8], Zahid Hussain[3], Yulin Chen[11], Miguel M. Ugeda[12,13], Zhi Liu[4,5], Xiaoming Xie[4,5], Thomas P. Devereaux[1,2], Michael F. Crommie[6,14,15], Sung-Kwan Mo[3*] and Zhi-Xun Shen[1,2*]

A quantum spin Hall (QSH) insulator is a novel two-dimensional quantum state of matter that features quantized Hall conductance in the absence of a magnetic field, resulting from topologically protected dissipationless edge states that bridge the energy gap opened by band inversion and strong spin–orbit coupling[1,2]. By investigating the electronic structure of epitaxially grown monolayer 1T′-WTe_2 using angle-resolved photoemission (ARPES) and first-principles calculations, we observe clear signatures of topological band inversion and bandgap opening, which are the hallmarks of a QSH state. Scanning tunnelling microscopy measurements further confirm the correct crystal structure and the existence of a bulk bandgap, and provide evidence for a modified electronic structure near the edge that is consistent with the expectations for a QSH insulator. Our results establish monolayer 1T′-WTe_2 as a new class of QSH insulator with large bandgap in a robust two-dimensional materials family of transition metal dichalcogenides (TMDCs).

A two-dimensional (2D) topological insulator (TI), or a quantum spin Hall insulator, is characterized by an insulating bulk and a conductive helical edge state, in which carriers with different spins counter-propagate to realize a geometry-independent edge conductance $2e^2/h$ (refs 1,2). The only scattering channel for such helical edge current is back scattering, which is prohibited by time reversal symmetry, making QSH insulators a promising material candidate for spintronic and other applications.

The prediction of the QSH effect in HgTe quantum wells sparked intense research efforts to realize the QSH state[3–11]. So far only a handful of QSH systems have been fabricated, mostly limited to quantum well structures of three-dimensional (3D) semiconductors such as HgTe/CdTe (ref. 3) and InAs/GaSb (ref. 6). Edge conduction consistent with a QSH state has been observed[3,6,12]. However, the behaviour under a magnetic field, where time reversal symmetry is broken, cannot be explained within our current understanding of the QSH effect[13,14]. There have been continued efforts to predict and investigate other material systems to further advance the understanding of this novel quantum phenomenon[5,7–9,15]. So far, it has been difficult to make a robust 2D material with a QSH state, a platform needed for widespread study and application. The small bandgaps exhibited by many candidate systems, as well as their vulnerability to strain, chemical adsorption, and element substitution, make them impractical for advanced spectroscopic studies or applications. For example, a QSH insulator candidate stanene, a monolayer analogue of graphene for tin, grown on Bi_2Se_3 becomes topologically trivial due to the modification of its band structure by the underlying substrate[11,16]. Free-standing Bi film with 2D bonding on a cleaved surface has shown edge conduction[9], but its topological nature is still debated[17]. It takes 3D out-of-plane bonding with the substrate and large strain (up to 18%) to open a bulk energy gap in monolayer bismuth[15]. Such 3D bonding structure may induce similar surface issues as seen in 3D semiconductor QSH systems. Monolayer FeSe grown on a $SrTiO_3$ substrate has also emerged as a model system to support both QSH and superconductivity. However, due to doping from the substrate, the Fermi energy (E_F) is more than 500 meV higher than the non-trivial gap, making it less practical for applications[18].

1T′ phase monolayer TMDCs MX_2, M = (W, Mo) and X = (Te, Se, S), are theoretically predicted to be a promising new class of QSH insulators with large bandgap[10]. Among them, WTe_2 is the only one for which the 1T′ phase is most energetically favoured. Realization of a QSH insulator in 2D TMDCs would be a breakthrough as this is a robust family of materials with none of the complications from surface/interface dangling bonds that are seen in 3D semiconductors, enabling a broad range of study and application of QSH physics. In this work, we report a successful growth of monolayer 1T′-WTe_2 using molecular beam epitaxy (MBE) on a bilayer graphene (BLG) substrate. In-situ ARPES measurements clearly show the band inversion and the opening of a 55 meV bulk bandgap, which is an

[1]Stanford Institute for Materials and Energy Sciences, SLAC National Accelerator Laboratory, 2575 Sand Hill Road, Menlo Park, California 94025, USA. [2]Geballe Laboratory for Advanced Materials, Departments of Physics and Applied Physics, Stanford University, Stanford, California 94305, USA. [3]Advanced Light Source, Lawrence Berkeley National Laboratory, Berkeley, California 94720, USA. [4]State Key Laboratory of Functional Materials for Informatics, Shanghai Institute of Microsystem and Information Technology, Chinese Academy of Sciences, Shanghai 200050, China. [5]School of Physical Science and Technology, Shanghai Tech University, Shanghai 200031, China. [6]Department of Physics, University of California at Berkeley, Berkeley, California 94720, USA. [7]Max Plank POSTECH Center for Complex Phase Materials, POSTECH, Pohang 37673, Korea. [8]Department of Physics, Pusan National University, Busan 46241, Korea. [9]Pohang Accelerator Laboratory, POSTECH, Pohang 37673, Korea. [10]Stanford Synchrotron Radiation Lightsource, SLAC National Accelerator Laboratory, 2575 Sand Hill Road, Menlo Park, California 94025, USA. [11]Department of Physics and Clarendon Laboratory, University of Oxford, Parks Road, Oxford OX1 3PU, UK. [12]Ikerbasque, Basque Foundation for Science, 48013 Bilbao, Spain. [13]CIC nanoGUNE, 20018 San Sebastián, Spain. [14]Materials Sciences Division, Lawrence Berkeley National Laboratory, Berkeley, California 94720, USA. [15]Kavli Energy Nano Sciences Institute, University of California and Lawrence Berkeley National Laboratory, Berkeley, California 94720, USA. †These authors contributed equally to this work. *e-mail: skmo@lbl.gov; zxshen@stanford.edu

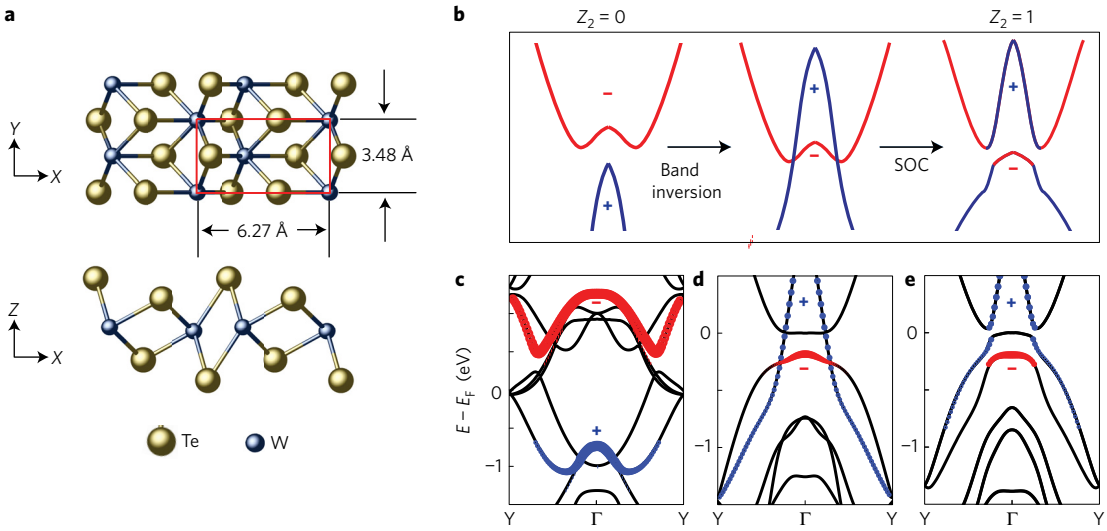

Figure 1 | Topological phase transition in 1T′-WTe_2. a, Crystal structure of 1T′-WTe_2. The doubled period due to the spontaneous lattice distortion from 1T phase is indicated by the red rectangle. **b**, Schematic diagram to show the bulk band evolution from a topologically trivial phase, to a non-trivial phase, and then to a bulk band opening due to SOC. **c**–**e**, Calculated band structures for WTe_2 to show the evolution from 1T-WTe_2 along the Γ–Y direction (**c**), 1T′-WTe_2 without SOC (**d**) and 1T′-WTe_2 with SOC (**e**). Red and blue dotted bands highlight the two bands involved in band inversion, which mainly contain the $5d_{z^2}$ and $5d_{xz}$ orbital contents, respectively. + and − signs denote the parity of the Bloch states at the Γ point.

order of magnitude larger than gaps seen in quantum wells of 3D semiconductors[3,6]. Scanning tunnelling spectroscopy (STS) spectra show evidence of the insulating bulk and conductive edge nature of 1T′-WTe_2. Our results thus provide compelling experimental evidence of a QSH insulator phase in monolayer 1T′-WTe_2.

Figure 1a presents the crystal structure of monolayer 1T′-WTe_2. MX_2 has three typical phases, namely 2H, 1T and 1T′. 1T-WTe_2 is composed of three hexagonally packed atomic layers in an ABC stacking. The metal atoms are in octahedral coordination with the chalcogen atoms. This is not a stable phase in free-standing form and undergoes a spontaneous lattice distortion into the 1T′ phase via a doubling of the periodicity in the X direction. W atoms are dislocated from the original octahedral positions to form a zigzag chain in the Y direction.

The lattice distortion from the 1T phase to the 1T′ phase induces band inversion and causes 1T′-WTe_2 to become topologically non-trivial[10,19,20]. Figure 1b schematically summarizes this topological phase transition in 1T′-WTe_2. Without spin–orbit coupling (SOC), the inverted bands cross at a momentum point along the Γ–Y direction, forming a Dirac cone. Strong SOC lifts the degeneracy at the Dirac point, opening a bulk bandgap. Following the bulk-boundary correspondence[21,22], the helical edge state is guaranteed by the gapped topologically non-trivial bulk band structure.

Our first-principles band structure calculations for 1T- and 1T′-WTe_2 are presented in Fig. 1c–e, which is generally consistent with the literature[10,20,23]. The key bands for the band inversion with opposite parities are marked to track their evolution. In 1T-WTe_2, the bands from $5d_{xz}$ and $5d_{z^2}$ orbitals of W are separated by the E_F (Fig. 1c). Due to the symmetry breaking through the lattice distortion from 1T to 1T′, these orbitals hybridize substantially. Figure 1d shows that the d_{z^2} orbital is lowered below E_F whereas the d_{xz} orbital lifts in the opposite direction near the Γ point. Because these two inverted bands have different parities at the Γ point, the Z_2 invariant ν, in which $(-1)^\nu$ determined by the product of all occupied band parity eigenvalues[24], changes from 0 to 1. The valence band maximum in the 1T′ phase is mainly from the W d_{yz} orbital, with an even parity at the Γ point. When its degeneracy with the d_{xz} orbital in the 1T phase is lifted by the lattice distortion, the band stays below E_F and does not involve in the band inversion. With the inclusion of SOC (Fig. 1e), the bands further hybridize with each other and the degeneracies at the Dirac cones formed by the band inversion are lifted, opening a bandgap in the bulk states. We note here that different calculation methods give different estimates on the size of the bandgap for strain-free 1T′-WTe_2 monolayers. The generalized-gradient approximation (Perdew–Burke–Ernzerhof, PBE) usually underestimates the bandgap and gives a negative bandgap value[10], while PBE with hybrid function (HSE06) gives a positive value[23].

Figure 2 summarizes the MBE growth and the characterization of 1T′-WTe_2 on BLG/SiC(0001) (see Methods for the details of the growth condition). The reflection high-energy electron diffraction (RHEED) pattern of the BLG substrate and the monolayer 1T′-WTe_2 are presented in Fig. 2a. Clean vertical line profiles after the deposition of W and Te clearly indicate the layer-by-layer growth mode. Using the lattice constant of BLG ($a = 2.46$ Å) as a reference, the lattice constant of the grown film is estimated to be ∼6.3 Å ± 0.2 Å, consistent with the expected value for monolayer 1T′-WTe_2 (ref. 23). The angle-integrated core level photoemission spectrum (Fig. 2b) exhibits the characteristic peaks of W and Te for the 1T′ phase. Two differently coordinated types of Te contribute two sets of Te 4d peaks, while the clean doublet feature of the W 4f peaks indicates a pure 1T′ phase rather than a mixed phase of 1T′ and 1H (ref. 25). Figure 2c is an atomically resolved scanning tunnelling microscopy (STM) image of 1T′-WTe_2, from which a ∼7.5° angle distortion is observed, which is universal in bulk 1T′ phase MX_2 (refs 25,26). Supplementary Fig. 5a,b show a typical morphology of the 1T′-WTe_2 on BLG substrate. A typical diameter for a branched island is ∼50 nm, with branches having sizes larger than 20 nm × 20 nm. Since the growth is edge-diffusion limited, the edge geometry is random.

The measured Fermi surface (FS) from the *in-situ* ARPES is shown in Fig. 2e. Due to the symmetry mismatch between the two-fold rotational symmetry of the sample and the three-fold symmetry of the substrate, there exist three energetically equivalent domains rotated by 120° with respect to each other, and each domain contributes two electron pockets along the Γ–Y direction of their respective Brillouin zones[27]. The experimental band dispersion along Γ–Y cutting the FS electron pockets is inevitably superposed with the contributions from Γ–P and Γ–P'. However, as shown in Fig. 2f–h, the valence bands from Γ–P' and Γ–P directions are enclosed by the Γ–Y band. Therefore, the existence of multiple

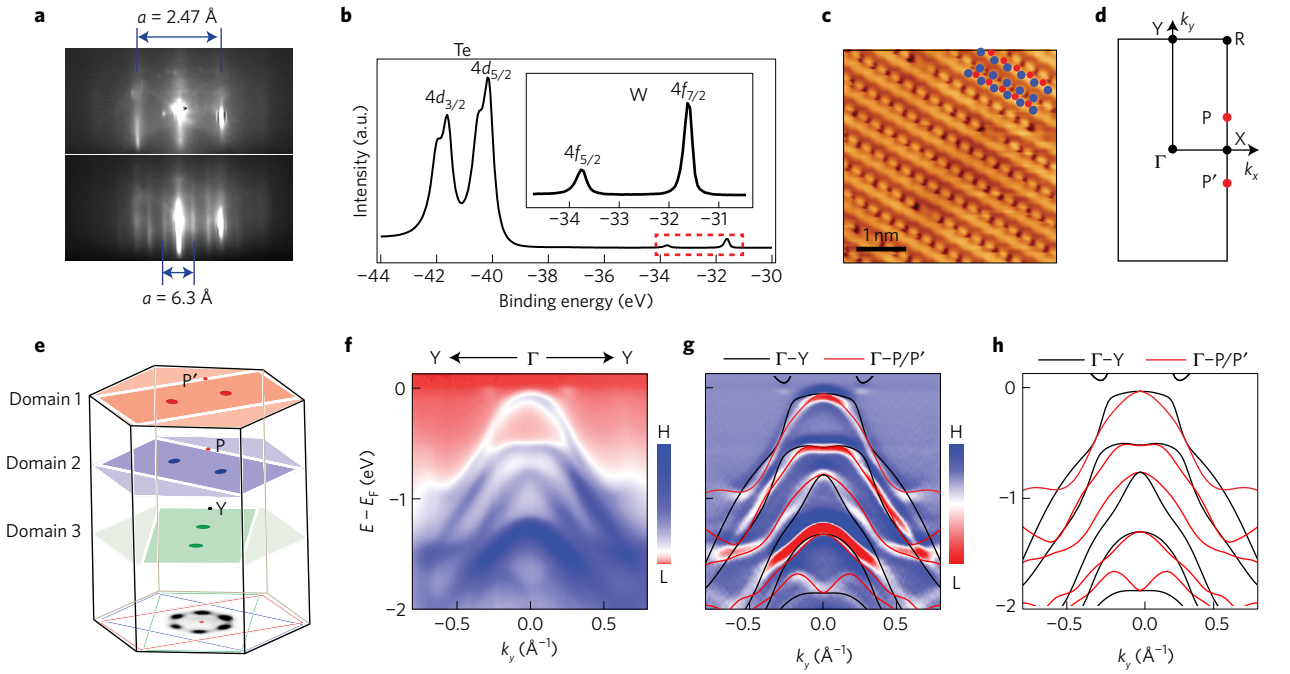

Figure 2 | Characterization of epitaxially grown 1T′-WTe_2 and overall electronic structure from ARPES. a, RHEED pattern of graphene substrate (top) and sub-monolayer 1T′-WTe_2 (bottom). **b**, Core level spectra of 1T′-WTe_2. The inset is a close-up for the region marked by the red dashed rectangle. **c**, Atomically resolved STM topographic image of 1T′-WTe_2. Blue and red dots represent W and Te atoms, respectively. **d**, Brillouin zone of 1T′-WTe_2. Time reversal invariant momenta Γ, X, Y, R are labelled by black dots. **e**, Fermi surface map of 1T′-WTe_2. The intensity is integrated within a ±10 meV window around E_F. There are three domains rotated with respect to each other by 120° due to difference in the symmetry of the sample and the substrate. The measured data along the Γ–Y high-symmetry direction is unavoidably mixed with the signals from the Γ–P and P′ directions. The schematic contributions from different domains are represented by different colour panes above the real Fermi surface map at the bottom. **f**, Overall band structure measured along the experimental Γ–Y direction. **g**, Second derivative spectra to enhance low-intensity features. The overlaid black lines are the calculated band structure along the Γ–Y direction. **h**, Calculated band structure along the Γ–Y (black) and Γ–P/P′ (red) directions, respectively. The low-energy electronic structure around the Γ point is dominated by the contributions from the Γ–Y bands.

domains does not affect the characterization of the gap size and the separation between valence and conduction bands. Overall band structure measured with ARPES (Fig. 2f,g) gives a nice agreement with the HSE06 calculation (Fig. 2g), demonstrating the 1T′ nature and the high quality of our thin-film samples. The predicted band inversion in 1T′-WTe_2 is well established experimentally by a polarization-dependent ARPES measurement, from which one can clearly distinguish in- and out-of-plane orbital characters and their inversion around the Γ point (Supplementary Figs 1 and 2). This indicates the non-trivial topology of 1T′-WTe_2.

The signature of strong SOC in 1T′-WTe_2 is the lifting of state degeneracy at the Dirac cones along the Γ–Y direction, resulting in an opening of the bulk gap as illustrated in Fig. 3a. This can be seen more clearly in the energy distribution curves (EDCs) extracted at the valence band top and the conduction band bottom. Since the ARPES data in Fig. 2 show only faint tails of the bulk conduction band, we deposited potassium (K) onto the surface to raise E_F (ref. 28) and make the conduction band more clearly visible to ARPES. Figure 3b focuses only on the low-energy electronic structure of surface K-doped 1T′-WTe_2, with E_F raised ∼70 meV to reveal the conduction band bottom more clearly. The corresponding EDCs in Fig. 3c show that the conduction band and the valence band are well separated from each other. To quantify the size of the bandgap, we extracted two EDCs from the momentum positions at the conduction band bottom and valence band top, labelled by the dashed lines in Fig. 3b, and overlaid them in Fig. 3d. The red and green peaks in Fig. 3d correspond to the energy positions of the conduction band bottom and the valence band top, respectively. We estimate the size of the bandgap to be 55 ± 20 meV and 45 ± 20 meV in intrinsic and K-doped samples, respectively (Supplementary Fig. 3). This is in clear contrast to the bulk 1T′-WTe_2, which is a semimetal with a complex band structure near E_F exhibiting multiple Fermi pockets[29]. The stacking of energy momentum dispersions with fine momentum steps parallel to the Γ–Y direction (Fig. 3e,f) further establish the effect of SOC by showing that the gap never closes for any momentum across the FS.

Now that we have established band inversion and the opening of a bandgap due to the strong SOC, the remaining signature of a QSH insulator is the conductive edge state in contrast to the insulating bulk, which can be better examined by STS. Figure 4a shows the local differential conductance (dI/dV) spectrum taken at a point far away from the WTe_2 edges, which represents the bulk local density of states (LDOS). The peak positions in dI/dV are in good agreement with the band edges found in ARPES. The agreement between ARPES and STS further extends to the size of the gap, as the mean gap size determined by STS is 56 ± 14 meV (Supplementary Fig. 6). In contrast to the gap in the bulk, dI/dV at a 1T′-WTe_2 edge is very different, showing a 'V-shape' spectrum with states filling in the bulk gap (Fig. 4b), which may indicate the existence of a conductive edge state. Indeed, similar dI/dV spectral line shapes have been reported for other topological systems with distinct edge states[15,30] and have been attributed to the one-dimensional (1D) nature of the edge states and the emergence of a Luttinger liquid[15]. Figure 4c shows dI/dV as a function of energy and distance away from an edge, which demonstrates that the V-shaped conductance is localized at the edge of the WTe_2. We observe that such localized edge states run continuously along our sample edges (Supplementary Fig. 7), with only small variations in the fine details of the spectra, regardless of the size, shape, and edge roughness of samples. This provides evidence of the edge state's topologically non-trivial nature[30,31].

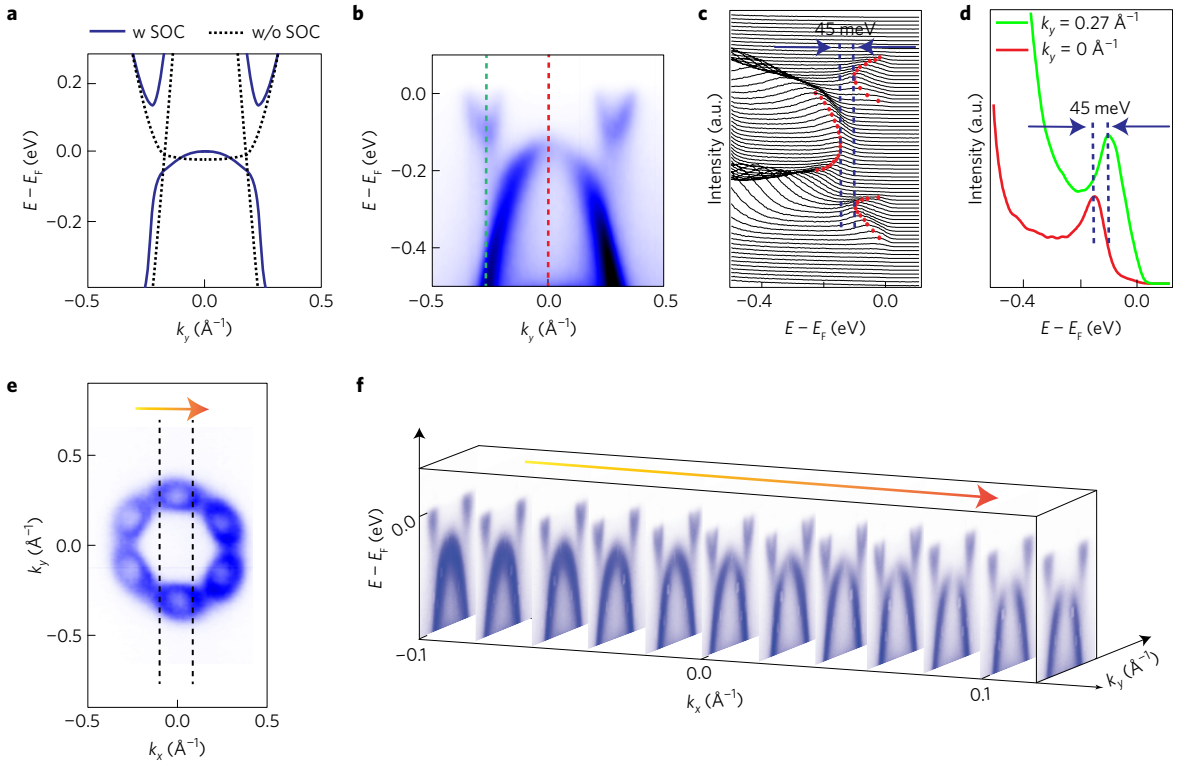

Figure 3 | Bandgap opening in monolayer 1T′-WTe_2. a, Calculated band structure along the Γ–Y direction. **b**, ARPES data along the Γ–Y direction taken from surface K-doped sample. **c**, EDCs for the data in **b**. **d**, EDCs from the momentum positions marked with green and red lines in **b**. The green line corresponds to the conduction band bottom and the red line corresponds to the valence band top. **e**, Fermi surface map of K-doped sample. Six electron pockets are due to the three rotational domains as explained for Fig. 2e. We focus only on the FS from a single domain. **f**, Stacking plot of cuts between the parallel dotted lines labelled in **e**.

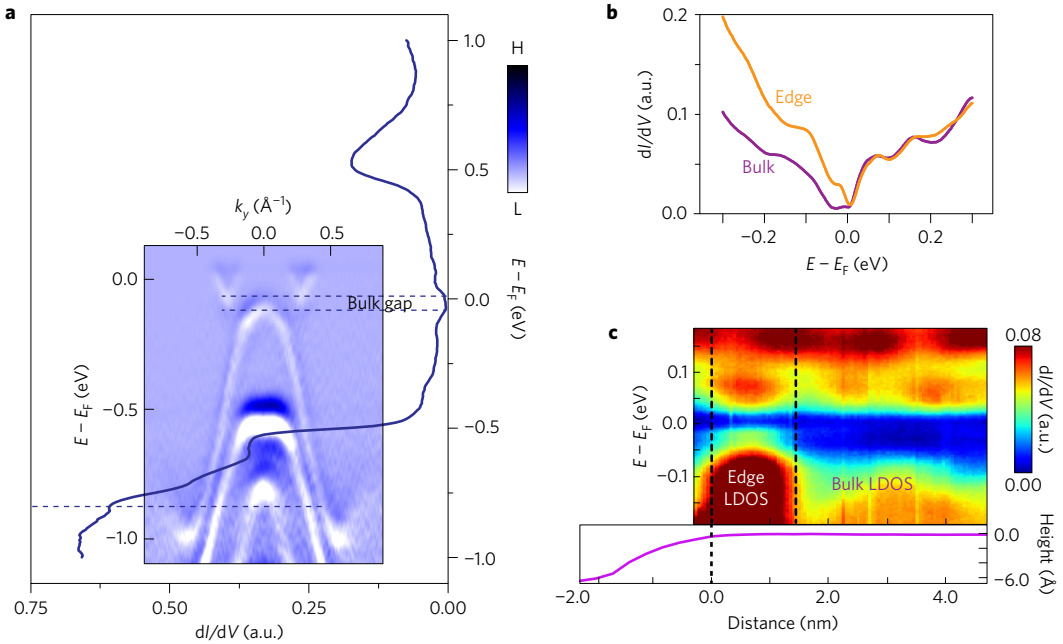

Figure 4 | Tunnelling spectroscopy in the bulk and at the edge of 1T′-WTe_2. a, STM d*I*/d*V* spectrum acquired in the bulk of monolayer 1T′-WTe_2. The inset is the high-symmetry ARPES cut along the Γ–Y direction aligned in energy with the STS spectrum (acquired from a K-doped sample). Since the surface K-doping raises the position of E_F by 70 meV, the whole ARPES spectrum is shifted by that amount for proper comparison with STS. **b**, Representative d*I*/d*V* spectra taken at the edge (orange) and in the bulk (purple), respectively. **c**, d*I*/d*V* spectra taken across the step edge of a 1T′-WTe_2 monolayer island (top), and corresponding height profile (bottom).

By combining ARPES and STS results, we provide strong evidence supporting the direct observation of all the characteristic electronic properties of a QSH state with a large energy gap in 1T′-WTe_2, confirming the theoretical prediction[10]. Such a robust platform for a QSH insulator in 2D TMDCs should provide new opportunities for fundamental studies and novel device

applications. Since TMDCs are inert, widely available, can be exfoliated for transport experiments, and be made into few-layer and van der Waals heterostructure devices, we expect them to be the material of choice for a much expanded, multimodal effort to understand and utilize QSH systems.

Methods

Methods, including statements of data availability and any associated accession codes and references, are available in the online version of this paper.

Received 23 October 2016; accepted 12 May 2017; published online 26 June 2017

References

1. Kane, C. L. & Mele, E. J. Quantum spin Hall effect in graphene. *Phys. Rev. Lett.* **95,** 226801 (2005).
2. Bernevig, B. A., Hughes, T. L. & Zhang, S.-C. Quantum spin Hall effect and topological phase transition in HgTe quantum wells. *Science* **314,** 1757–1761 (2006).
3. König, M. *et al*. Quantum spin Hall insulator state in HgTe quantum wells. *Science* **318,** 766–770 (2007).
4. Liu, C. *et al*. Quantum spin Hall effect in inverted type-II semiconductors. *Phys. Rev. Lett.* **100,** 236601 (2008).
5. Liu, Z. *et al*. Stable nontrivial Z_2 topology in ultrathin Bi (111) films: a first-principles study. *Phys. Rev. Lett.* **107,** 136805 (2011).
6. Knez, I., Du, R.-R. & Sullivan, G. Evidence for helical edge modes in inverted InAs/GaSb quantum wells. *Phys. Rev. Lett.* **107,** 136603 (2011).
7. Xu, Y. *et al*. Large-gap quantum spin Hall insulators in tin films. *Phys. Rev. Lett.* **111,** 136804 (2013).
8. Weng, H., Dai, X. & Fang, Z. Transition-metal pentatelluride $ZrTe_5$ and $HfTe_5$: a paradigm for large-gap quantum spin Hall insulators. *Phy. Rev. X* **4,** 011002 (2014).
9. Drozdov, I. K. *et al*. One-dimensional topological edge states of bismuth bilayers. *Nat. Phys.* **10,** 664–669 (2014).
10. Qian, X., Liu, J., Fu, L. & Li, J. Quantum spin Hall effect in two-dimensional transition metal dichalcogenides. *Science* **346,** 1344–1347 (2014).
11. Zhu, F.-F. *et al*. Epitaxial growth of two-dimensional stanene. *Nat. Mater.* **14,** 1020–1025 (2015).
12. Nowack, K. C. *et al*. Imaging currents in HgTe quantum wells in the quantum spin Hall regime. *Nat. Mater.* **12,** 787–791 (2013).
13. Ma, E. Y. *et al*. Unexpected edge conduction in mercury telluride quantum wells under broken time-reversal symmetry. *Nat. Commun.* **6,** 7252 (2015).
14. Fabrizio, N. *et al*. Edge transport in the trivial phase of InAs/GaSb. *New J. Phys.* **18,** 083005 (2016).
15. Reis, F. *et al*. Bismuthene on a SiC substrate: a candidate for a new high-temperature quantum spin Hall paradigm. Preprint at http://adsabs.harvard.edu/abs/2016arXiv160800812R (2016).
16. Xu, Y., Tang, P. & Zhang, S.-C. Large-gap quantum spin Hall states in decorated stanene grown on a substrate. *Phys. Rev. B* **92,** 081112 (2015).
17. Takayama, A. *et al*. One-dimensional edge states with giant spin splitting in a bismuth thin film. *Phys. Rev. Lett.* **114,** 066402 (2015).
18. Wang, Z. F. *et al*. Topological edge states in a high-temperature superconductor FeSe/$SrTiO_3$(001) film. *Nat. Mater.* **15,** 968–973 (2016).
19. Keum, D. H. *et al*. Bandgap opening in few-layered monoclinic $MoTe_2$. *Nat. Phys.* **11,** 482–486 (2015).
20. Choe, D.-H., Sung, H.-J. & Chang, K. J. Understanding topological phase transition in monolayer transition metal dichalcogenides. *Phys. Rev. B* **93,** 125109 (2016).
21. Essin, A. M. & Gurarie, V. Bulk-boundary correspondence of topological insulators from their respective Green's functions. *Phys. Rev. B* **84,** 125132 (2011).
22. Hasan, M. Z. & Kane, C. L. Colloquium: topological insulators. *Rev. Mod. Phys.* **82,** 3045–3067 (2010).
23. Zheng, F. *et al*. On the quantum spin Hall gap of monolayer 1T'-WTe_2. *Adv. Mater.* **28,** 4845–4851 (2016).
24. Fu, L. & Kane, C. L. Topological insulators with inversion symmetry. *Phys. Rev. B* **76,** 045302 (2007).
25. Das, P. K. *et al*. Layer-dependent quantum cooperation of electron and hole states in the anomalous semimetal WTe_2. *Nat. Commun.* **7,** 10847 (2016).
26. Hla, S. W., Marinković, V., Prodan, A. & Muševič, I. STM/AFM investigations of β-$MoTe_2$, α-$MoTe_2$ and WTe_2. *Surf. Sci.* **352–354,** 105–111 (1996).
27. Ugeda, M. M. *et al*. Characterization of collective ground states in single-layer $NbSe_2$. *Nat. Phys.* **12,** 92–97 (2016).
28. Zhang, Y. *et al*. Direct observation of the transition from indirect to direct bandgap in atomically thin epitaxial $MoSe_2$. *Nat. Nanotech.* **9,** 111–115 (2014).
29. Jiang, J. *et al*. Signature of strong spin-orbital coupling in the large nonsaturating magnetoresistance material WTe_2. *Phys. Rev. Lett.* **115,** 166601 (2015).
30. Pauly, C. *et al*. Subnanometre-wide electron channels protected by topology. *Nat. Phys.* **11,** 338–343 (2015).
31. Lin, H. *et al*. Topological dangling bonds with large spin splitting and enhanced spin polarization on the surfaces of Bi_2Se_3. *Nano Lett.* **13,** 1915–1919 (2013).

Acknowledgements

The ARPES and thin film growth works at the Stanford Institute for Materials and Energy Sciences and Stanford University are supported by the Office of Basic Energy Sciences, Division of Materials Science and AFOSR Grant FA9550-14-1-0277 through the University of Washington that support the ALS activity by the Stanford team. Research performed at ALS (thin film growth and ARPES) is supported by the Office of Basic Energy Sciences, US DOE under Contract No. DE-AC02-05CH11231. SSRL is supported by the Office of Basic Energy Sciences, US DOE under Contract No. DE-AC02-76SF00515. Scanned probe measurements were supported by the VdW Heterostructure Program (KCWF16) (STM spectroscopy) funded by the Office of Basic Energy Sciences, US DOE under Contract No. DE-AC02-05CH11231, as well as by National Science Foundation award EFMA-1542741 (surface treatment and topographic characterization). Z.L. is supported by the National Natural Science Foundation of China (11227902). S.T. acknowledges support by the CPSF-CAS Joint Foundation for Excellent Postdoctoral Fellows. J.J. and C.-C.H. acknowledge the support of the NRF, Korea (No. 2011-0030787 and No. 2017R1A2B2003928). H.R. and C.H. acknowledge the support from the NRF, Korea through Max Planck Korea/POSTECH Research Initiative (No. 2011-0031558) and Basic Science Research Program (No. 2015R1C1A1A01053065). M.M.U. acknowledges financial support from Spanish MINECO Grant No. MAT2014-60996-R. A portion of the computational work was performed using the resources of the National Energy Research Scientific Computing Center (NERSC) supported by the US Department of Energy, Office of Science, under Contract No. DE-AC02-05CH11231.

Author contributions

S.T., C.Z., S.-K.M. and Z.-X.S. proposed and designed the research. S.T. performed the MBE growth. S.T. and C.Z. carried out the ARPES measurements and analysed the ARPES data with help from J.J., H.R., S.-K.M., M.H. and D.L. D.W., Z.P., H.-Z.T., S.K., M.M.U. and M.F.C. performed the STM measurements and analysed STM data. C.J., M.C., B.M. and T.P.D. carried out the density functional calculations and provided theoretical support. S.T., S.-K.M., D.W. and Z.-X.S. wrote the manuscript with contributions and comments from all authors.

Additional information

Supplementary information is available in the online version of the paper. Reprints and permissions information is available online at www.nature.com/reprints. Publisher's note: Springer Nature remains neutral with regard to jurisdictional claims in published maps and institutional affiliations. Correspondence and requests for materials should be addressed to S.-K.M. or Z.-X.S.

Competing financial interests

The authors declare no competing financial interests.

Methods

Thin-film growth. The monolayer 1T′-WTe_2 films were grown by MBE on bilayer graphene (BLG) epitaxially grown on 6H-SiC[32]. Growth was performed at Beamline 10.0.1, Advanced Light Source, Lawrence Berkeley National Laboratory. The base pressure of the MBE chamber was $\sim 4 \times 10^{-10}$ torr. Ultrahigh-purity tellurium (99.999%) and tungsten (99.999%) was evaporated from an effusion cell and an electron beam evaporator, respectively. The flux ratio between tungsten and tellurium is set between 1:10 ∼ 1:20. We found that the quality of the sample does not depend much on the ratio. However, it depends critically on the substrate temperature. The substrate temperature was held at 280 °C during growth. The growth process was monitored by RHEED. The growth rate was ∼40 min per monolayer. After growth we annealed the sample at 300 °C for 2 h to improve the film quality[33].

ARPES measurement. *In-situ* ARPES measurements were performed at Beamline 10.0.1, Advanced Light Source, Lawrence Berkeley National Laboratory. ARPES data were acquired with a Scienta R4000 electron analyser at a temperature of 60 K. The energy and angular resolutions are set to be 18 meV and 0.1°, respectively. Two different photon polarizations were used. In the S-polarization, the electric field of the photon is perpendicular to the incidence plane defined by the sample normal and the photon momentum. In the P-polarization, the photon electric field is 10° out of the incidence plane. It is composed of both s polarized and p polarized light. The intensity ratio between the s polarization and p polarization is 17:83. We nonetheless refer to this as P-polarization, since the actual polarization is dominated by p polarized light. The spot size of the photon beam on the sample was ∼100 μm × 100 μm. The potassium used to perform a surface doping of the film was evaporated from a SAES Getters alkali metal dispenser.

STM measurement. To protect the film from an exposure to air during the transfer to the STM chamber, Te and Se capping layers with thicknesses of ∼100 nm were both deposited on the film (Te layer first) before taking the samples out of the ultrahigh-vacuum (UHV) system of Beamline 10.0.1. Annealing at 200 °C for half an hour was enough to remove the capping layer immediately before STM measurements after having introduced the sample into the STM UHV system. Scanning tunnelling spectroscopy (STS) measurements were performed at $T = 4.8$ K with platinum iridium tips calibrated against the Au(111) Shockley surface state. dI/dV measurements were obtained via lock-in detection of the a.c. tunnelling current induced by a 5 mV, 613.7 Hz modulation voltage applied to the STM tip.

Electronic structure calculations. The band structure and orbital content as presented in Fig. 1 are calculated using the full-potential linearized augmented plane wave method implemented in Wien2k. *Ab initio* calculations were performed in the framework of the Perdew–Burke–Ernzerhof (PBE) type generalized-gradient approximation (GGA) of density functional theory (DFT). The band structure calculations as presented in Figs 2g,h and 3a in the main text were calculated using the VASP package with projector augmented wave pseudo-potentials, using the Heyd–Scuseria–Ernzerhof (HSE06) exchange–correlation functional with spin–orbital coupling (SOC). The lattice constants and internal atom positions are optimized with the PBE exchange–correlation functional[10].

Data availability. The data that support the plots within this paper and other findings of this study are available from the corresponding author upon reasonable request.

References

32. Qingyan, W. *et al*. Large-scale uniform bilayer graphene prepared by vacuum graphitization of 6H-SiC(0001) substrates. *J. Phys. Condens. Matter* **25,** 095002 (2013).
33. Zhang, Y. *et al*. Giant phonon-induced conductance in scanning tunnelling spectroscopy of gate-tunable graphene. *Nat. Phys.* **4,** 627–630 (2008).